

Performance Gaps of Artificial Intelligence Models in Screening Mammography - Towards Fair and Interpretable Models

Linglin Zhang, MS¹, Beatrice Brown-Mulry, BS¹, Vineela Nalla, BS², InChan Hwang, MS¹, Judy Wawira Gichoya, MD³, Aimilia Gastounioti, PhD⁴, Imon Banerjee, PhD^{5,6}, Laleh Seyyed-Kalantari, PhD⁷, MinJae Woo, PhD¹, Hari Trivedi, MD³

1. School of Data Science and Analytics, Kennesaw State University, 3391 Town Point Dr NW, Kennesaw, GA 30144
2. Department of Information Technology, Kennesaw State University, 1100 South Marietta Pkwy, Marietta, GA 30060
3. Department of Radiology and Imaging Sciences, Emory University, 1364 E Clifton Rd NE, Atlanta, GA 30322
4. Computational Imaging Research Center, Washington University in St. Louis School of Medicine, 4525 Scott Avenue, St. Louis, MO 63110
5. Department of Radiology, Mayo Clinic Arizona, 13400 E Shea Blvd, Scottsdale, AZ 85259
6. School of Computing and Augmented Intelligence, Arizona State University, 699 S Mill Ave, Tempe, AZ 85281
7. Department of Electrical Engineering and Computer Science, York University, 4700 Keele St, Toronto, Ontario, Canada M3J 1P3

{lzhang23, bbrownmu, vnalla, ihwang}@students.kennesaw.edu
{judywawira, hari.trivedi}@emory.edu
a.gastounioti@wustl.edu
banerjee.imon@mayo.edu
lsk@yorku.ca
mwool@kennesaw.edu

Abstract

Even though deep learning models for abnormality classification can perform well in screening mammography, the demographic and imaging characteristics associated with increased risk of failure for abnormality classification in screening mammograms remain unclear. This retrospective study used data from the Emory BrEast Imaging Dataset (EMBED) including mammograms from 115,931 patients imaged at Emory University Healthcare between 2013 to 2020. Clinical and imaging data includes Breast Imaging Reporting and Data System (BI-RADS) assessment, region of interest coordinates for abnormalities, imaging features, pathologic outcomes, and patient demographics. Deep learning models including InceptionV3, VGG16, ResNet50V2, and ResNet152V2 were developed to distinguish between patches of abnormal tissue and randomly selected patches of normal tissue from the screening mammograms. The distributions of the training, validation and test sets are 29,144 (55.6%) patches of 10,678 (54.2%) patients, 9,910 (18.9%) patches of 3,609 (18.3%) patients, and 13,390 (25.5%) patches of 5,404 (27.5%) patients. We assessed model performance overall and within subgroups defined by age, race, pathologic outcome, and imaging characteristics to evaluate reasons for misclassifications. On the test set, a ResNet152V2 model trained to classify normal versus abnormal tissue patches achieved an accuracy of

92.6% (95%CI=92.0-93.2%), and area under the receiver operative characteristics curve 0.975 (95%CI=0.972-0.978). Imaging characteristics associated with higher misclassifications of images include higher tissue densities (risk ratio [RR]=1.649; p=.010, BI-RADS density C and RR=2.026; p=.003, BI-RADS density D), and presence of architectural distortion (RR=1.026; p<.001). Small but statistically significant differences in performance were observed by age, race, pathologic outcome, and other imaging features (p<.001).

Introduction

Breast cancer is the most common cancer in women and causes 42,000 deaths each year in the United States (1). Early detection via screening mammography has been shown to reduce morbidity and mortality of breast cancers by 38–48% through the recognition of abnormalities such as masses, calcification, asymmetries, and architectural distortions (ADs) (2-4). However, there is significant resource usage for detecting a relatively small number of cancers - for every 1,000 women screened, approximately 100 are recalled, and 30-40 are biopsied for the detection of only 5 cancers (5). This is largely due to the similar imaging appearance of many benign and malignant findings which necessitates repeat imaging and/or biopsy for definitive diagnosis. Improving differentiation of benign and malignant findings on screening mammography has potential to reduce wastage and decrease patient morbidity (3, 6, 7).

Deep learning techniques have been developed to assist radiologists in interpreting mammograms with many results showing systems that meet or exceed radiologists (8-15). The detection of abnormalities in mammography can be described as two steps: (1) detection of a potential abnormal region of interest (ROI); (2) classification of abnormalities according to image characteristics or likelihood of malignancy (6, 10-19). However, the performance of abnormality detection models has been described broadly – across multiple imaging features, breast densities, and patient demographics without the ability to evaluate performance on individual subgroups, largely due to the lack of available granular datasets that include these features (20, 21). This may lead to potential bias and unintended harm from AI models that to be underperformed for certain patient subgroups (e.g., race and age) (22, 23), cancer subtypes, or imaging findings (24). Such biases lead to lack of trust in the AI models in medical imaging as these models are deployed in clinics.

In this paper, we train a model for classification of normal versus abnormal patches of tissue on mammography and present a post-hoc analysis to identify imaging, pathologic, and demographic characteristics that result in model underperformance and could interfere with abnormality detection in screening mammography.

Materials and Methods

The experiment includes two sequential parts: (1) training multiple comparative deep learning models and validate, selecting the best model and acquire the testing prediction result; (2) statistically analyzing the correct and incorrect prediction by the models to identify clinical and demographical characteristics of patient groups vulnerable to misclassification, Figure 1.

Data Preparation

In this retrospective study, we used the EMory BrEast imaging Dataset (EMBED) (25) which contains clinical and imaging data for 3.4M mammogram images from 383,379 screening and diagnostic exams of 115,931 patients from 2013 to 2020 at a single institution. EMBED includes demographics, imaging features, pathologic outcomes, and Breast Imaging Reporting and Data System (BI-RADS) (26) densities and scores for screening and diagnostic exams. ROIs annotated by the radiologist during original interpretation are also available, predominantly for abnormal screening (BI-RADS 0) exams.

An overview of the data preparation is shown in Figure 2. For this study, we used only full field digital mammograms (FFDM). Positive patches were defined as ROIs annotated on BIRADS 0 images and were labeled with imaging features (mass, calcification, AD, asymmetry) and pathologic outcome (never biopsied, benign, or malignant). Negative image patches were generated from two sources: (1) random patches localized inside the breast tissue area avoiding any pixel in all annotated ROI(s) in a BI-RADS 0 image; (2) random patches localized inside the breast tissues from negative screening images (BI-RADS 1 and 2) as shown in Figure 3. Breast tissues were decided as pixels with non-zero values, where zero-valued pixels were regarded as backgrounds. The negative patch generating algorithm randomly cropped rectangular regions, until the percentage of background area pixels within the cropped area is less than a threshold of 10%. Negative patch sizes were generated to match the distribution of positive patches to avoid confounding. Patches greater than 512×512 were downsampled to less than 512×512 while maintaining aspect ratio. All patches were then zero-padded to be 512×512 pixels for consistent input size for the convolutional neural network (CNN). Patch sizes ranged from 53×76 to 2379×2940 with median size of 360×437. The final dataset was randomly divided at the patient level to prevent leakage, and consisted of 10,678 patients and 29,144 patches (55.6%) for training; 3,609 patients and 9,910 patches (18.9%) for validation; and 5,404 patients and 13,390 patches (25.5%) for testing.

Patch Classifier Model Training

Guided by previous studies, we tested four common CNN architectures enhanced by transfer learning, InceptionV3 (27), VGG16 (28), ResNet50V2 (29), and ResNet152V2 (30), to ensure the state-of-the-art performance in binary patch classification (31), with the same training, validation, and testing sets. Preliminary results demonstrated top performance by ResNet152V2 (Table 2), so this architecture was utilized throughout the study. Input layers were adjusted to accept 512×512-pixel resolution PNG files, followed by ResNet152V2 classifier pretrained on the ImageNet dataset (32), with the

additional layers including a trainable batch normalization layer. The following deep neural network constituents included a dense layer with ReLU activation (33), a dropout layer, three dense layers with ReLU, and final dense layer activated by Sigmoid function (34). Learning rate was optimized using Bayesian optimization (35), with the optimal model validation performance achieved at learning rate = 0.00588461.

Statistical Analysis

We performed bootstrapping using two hundred iterations ($n \in [1000, 13390]$) on the test set to evaluate the patch classifier performance by accuracy, area under the receiver operative characteristics curve (AUC), recall, precision, F1 score, false negative rate, and false positive rate. To evaluate hidden bias across subgroups, we assessed model performance by race – White, Black or Other; age groups – <50, 50-60, 60-70, and >70 years; BI-RADS tissue density – A, B, C, or D; pathology – never biopsied, cancer, or benign; and imaging features – mass, asymmetry, architectural distortion, or calcification. Subgroup AUC performance was compared using one-sided unpaired t test with a .025 level of significance built on Python 3.7.3 package SciPy 1.7.3.

In addition to assessing performance per patch, we also aggregated the results at the whole-image level. A correct image-level prediction was defined as having all patches within the image accurately classified, while an incorrect prediction was characterized by at least one misclassified patch in the image. For instance, an image with one accurately identified positive patch and one misclassified negative patch would yield an incorrect image-level prediction.

Model performance was evaluated across the same subgroups as above using risk ratio (RR) for image misclassification. Logistic regression was used to compare performance across groups using Python 3.7.3 using package StatsModels 0.13.2 with a .05 level of significance.

Results

Patient Characteristics

The patient age distribution was 59.02 ± 11.87 (standard deviation). There were 21,273 (40.6%) White patients, 22,321 (42.5%) Black patients, and 8,850 (16.9%) patients with other races. 16,387 (31.2%) patients were <50 years, 14,775 (28.2%) patients were 50-60 years, 12,490 (23.8%) patients were 60-70 years, and 8,792 (16.8%) patients were >70 years. Tissue density distribution for BI-RADS A to D was 6,050 (11.5%), 18,544 (35.4%), 23,218 (44.3%), and 4,632 (8.8%), respectively. Distribution of imaging features and pathologic outcomes are summarized in Table 1. Of note, counts by imaging feature could not be determined in the training and validation set. This is because, in this dataset, imaging features are assigned on a per *image* basis, not per *ROI*; therefore, in images with multiple lesions, it was not possible to determine

which imaging feature corresponded to which lesion. In the test dataset, this was resolved by selecting images with only one ROI so that lesion characteristics could be directly linked to each ROI.

Patch-level classification

The patch classification model built with ResNet152V2 achieved overall accuracy of 92.6% (95% CI = 92.0–93.2%), AUC of 0.975 (95% CI = 0.972-0.978), recall of 0.927 (95% CI = 0.919-0.935), precision of 0.912 (95% CI = 0.902-0.922), F1 score of 0.919 (95% CI = 0.913-0.925), false negative rate of 0.073 (95% CI = 0.065-0.081), false positive rate of 0.076 (95% CI = 0.068-0.084), on a test set of 13,390 patches from 5,404 patients. Table 3 shows detailed classification model performance across all patches, subgroups of race, age, tissue density, pathology outcome, and image findings. The receiver operative characteristics (ROC) curves by subgroups are in Figure 4.

Small but statistically significant differences were found between AUCs for all subgroups, including differences in performance across all races, better performance with decreasing age, better performance for density B compared to other densities, better performance for biopsied lesions (cancer or benign) as compared to never biopsied lesions, and worse performance for patches with architectural distortion. The detailed t-statistics and p-value for each pair of subgroups that were compared were demonstrated in Supplemental Table 1. The distribution of pathological outcomes of each image finding was shown in Supplemental Table 2.

Image-Level Classification

To evaluate the risk of misclassification on an image containing multiple positive or negative patches, we performed further analysis on misclassification at the image level (Figure 5). We found presence of two conditions to be associated with higher risk of misclassification when present in the image: (1) Images with BI-RADS density C and D are more likely to be exposed to misclassification compared to density A (RR=1.649; p=.010, BI-RADS density C and RR=2.026; p=.003, BI-RADS density D), and (2) images with architectural are more likely to be exposed to misclassification (RR=1.026; p<.001) than images with other features such as calcification, mass, or asymmetry.

Discussion

To our knowledge, this study is the first to investigate demographic, clinical, and imaging features that contribute to increased risk of failure for abnormality classification in screening mammograms. Our results show that there are both demographic and imaging characteristics that aggravate classification performance, which may lead to unexpected failures of abnormality object detection in mammograms.

We performed these evaluations both at the patch level and whole image level to better understand the effect of multiple lesions or other confounders in the data. At the patch level, we found sometimes small but statistically significant differences in model performance across all age, racial, imaging, and pathology subgroups. The largest differences in performance were observed between (BIRADS A vs. BIRADS D) with a 7.3% difference in accuracy, and between architectural distortion and asymmetry with a 10.4% difference in accuracy. At the image level, similar results showed increased relative risk for patients with higher tissue density C (RR=1.649; p=.010) and density D (RR=2.026; p=.003) and for patients with architectural distortion (RR=1.026; p<.001). Performance differences across breast density or imaging features is intuitive as increased breast density can mask and/or mimic lesions and architectural distortion is amongst the most difficult findings to identify clinically. Similarly, the small yet significant difference in performance between biopsied lesions (cancer or benign) versus never biopsied lesions is also intuitive since never biopsied lesions (BI-RADS 0 on screening, and BI-RADS 1 or 2 on diagnostic) were ultimately found to have no abnormality, indicating a false positive recall. However, the small but statistically significant differences in performance by race and age are more difficult to understand, particularly given the presence of adequate samples in the training data. This will require further investigation to evaluate for possible confounders.

The findings should be interpreted considering the study's methodological constraints. Our results suggest that certain imaging or patient characteristics could ultimately diminish a detection model's performance, however there is currently no publicly available object detection model available for digital mammograms for us to test this hypothesis. We hope to use this dataset to eventually train such a model. Another limitation is that we only included exams in subgroup analysis for which data was available and grouped imaging features and race into broad categories, which may obscure nuanced differences within these groups. Third, there may be confounding effects between imaging features, outcomes, and demographics that could affect model performance. Finally, this study was conducted at a single institution which focuses on a specific population in the southern United States and different disparities may be observed in different populations. However, our goal was not to train a generalizable model, but rather to evaluate a benchmark CNN classification architecture to identify potential sources of inequitable performance.

In conclusion, we developed an abnormality patch classifier for screening mammograms and performed subgroup analysis to investigate demographic, clinical, and imaging features that affect model performance. These features are likely to affect multiple CNN architectures for this task and may also affect object detection models with similar underlying architectures. These are important steps towards improving performance of fair and interpretable object detection models in mammography.

References

1. Basic Information About Breast Cancer. Centers for Disease Control and Prevention Web site 2022 [cited 2022 September 26th]. Available from: https://www.cdc.gov/cancer/breast/basic_info/index.htm#:~:text=Each%20year%20in%20the%20United,breast%20cancer%20than%20White%20women.
2. Broeders M, Moss S, Nyström L, Njor S, Jonsson H, Paap E, et al. The impact of mammographic screening on breast cancer mortality in Europe: a review of observational studies. *J Med Screen*. 2012;19 Suppl 1:14-25. doi: 10.1258/jms.2012.012078. PubMed PMID: 22972807.
3. Lehman CD, Arao RF, Sprague BL, Lee JM, Buist DS, Kerlikowske K, et al. National Performance Benchmarks for Modern Screening Digital Mammography: Update from the Breast Cancer Surveillance Consortium. *Radiology*. 2017;283(1):49-58. Epub 20161205. doi: 10.1148/radiol.2016161174. PubMed PMID: 27918707; PubMed Central PMCID: PMC5375631.
4. Balleyguier C, Ayadi S, Van Nguyen K, Vanel D, Dromain C, Sigal R. BIRADS classification in mammography. *Eur J Radiol*. 2007;61(2):192-4. Epub 20061211. doi: 10.1016/j.ejrad.2006.08.033. PubMed PMID: 17164080.
5. Lee JM, Arao RF, Sprague BL, Kerlikowske K, Lehman CD, Smith RA, et al. Performance of Screening Ultrasonography as an Adjunct to Screening Mammography in Women Across the Spectrum of Breast Cancer Risk. *JAMA Intern Med*. 2019;179(5):658-67. doi: 10.1001/jamainternmed.2018.8372. PubMed PMID: 30882843; PubMed Central PMCID: PMC6503561.
6. Ribli D, Horváth A, Unger Z, Pollner P, Csabai I. Detecting and classifying lesions in mammograms with Deep Learning. *Sci Rep*. 2018;8(1):4165. Epub 20180315. doi: 10.1038/s41598-018-22437-z. PubMed PMID: 29545529; PubMed Central PMCID: PMC5854668.
7. Kim HE, Kim HH, Han BK, Kim KH, Han K, Nam H, et al. Changes in cancer detection and false-positive recall in mammography using artificial intelligence: a retrospective, multireader study. *Lancet Digit Health*. 2020;2(3):e138-e48. Epub 20200206. doi: 10.1016/S2589-7500(20)30003-0. PubMed PMID: 33334578.
8. Rodríguez-Ruiz A, Krupinski E, Mordang JJ, Schilling K, Heywang-Köbrunner SH, Sechopoulos I, et al. Detection of Breast Cancer with Mammography: Effect of an Artificial Intelligence Support System. *Radiology*. 2019;290(2):305-14. Epub 20181120. doi: 10.1148/radiol.2018181371. PubMed PMID: 30457482.
9. Bae MS, Kim HG. Breast Cancer Risk Prediction Using Deep Learning. *Radiology*. 2021;301(3):559-60. Epub 20210907. doi: 10.1148/radiol.2021211446. PubMed PMID: 34491135.
10. Jiang J, Peng J, Hu C, Jian W, Wang X, Liu W. Breast cancer detection and classification in mammogram using a three-stage deep learning framework based on PAA algorithm. *Artif Intell Med*. 2022;134:102419. Epub 20221013. doi: 10.1016/j.artmed.2022.102419. PubMed PMID: 36462904.
11. Al-Masni MA, Al-Antari MA, Park JM, Gi G, Kim TY, Rivera P, et al. Simultaneous detection and classification of breast masses in digital mammograms via a deep learning YOLO-based CAD system. *Comput Methods Programs Biomed*. 2018;157:85-94. Epub 20180131. doi: 10.1016/j.cmpb.2018.01.017. PubMed PMID: 29477437.
12. Agarwal R, Díaz O, Yap MH, Lladó X, Martí R. Deep learning for mass detection in Full Field Digital Mammograms. *Comput Biol Med*. 2020;121:103774. Epub 20200422. doi: 10.1016/j.combiomed.2020.103774. PubMed PMID: 32339095.
13. Yala A, Lehman C, Schuster T, Portnoi T, Barzilay R. A Deep Learning Mammography-based Model for Improved Breast Cancer Risk Prediction. *Radiology*. 2019;292(1):60-6. Epub 20190507. doi: 10.1148/radiol.2019182716. PubMed PMID: 31063083.
14. Lotter W, Diab AR, Haslam B, Kim JG, Grisot G, Wu E, et al. Robust breast cancer detection in mammography and digital breast tomosynthesis using an annotation-efficient deep learning approach. *Nat Med*. 2021;27(2):244-9. Epub 20210111. doi: 10.1038/s41591-020-01174-9. PubMed PMID: 33432172; PubMed Central PMCID: PMC9426656.

15. Akselrod-Ballin A, Chorev M, Shoshan Y, Spiro A, Hazan A, Melamed R, et al. Predicting Breast Cancer by Applying Deep Learning to Linked Health Records and Mammograms. *Radiology*. 2019;292(2):331-42. Epub 20190618. doi: 10.1148/radiol.2019182622. PubMed PMID: 31210611.
16. Al-Antari MA, Al-Masni MA, Choi MT, Han SM, Kim TS. A fully integrated computer-aided diagnosis system for digital X-ray mammograms via deep learning detection, segmentation, and classification. *Int J Med Inform*. 2018;117:44-54. Epub 20180618. doi: 10.1016/j.ijmedinf.2018.06.003. PubMed PMID: 30032964.
17. Cao H, Pu S, Tan W, Tong J. Breast mass detection in digital mammography based on anchor-free architecture. *Comput Methods Programs Biomed*. 2021;205:106033. Epub 20210316. doi: 10.1016/j.cmpb.2021.106033. PubMed PMID: 33845408.
18. Kooi T, Litjens G, van Ginneken B, Gubern-Mérida A, Sánchez CI, Mann R, et al. Large scale deep learning for computer aided detection of mammographic lesions. *Med Image Anal*. 2017;35:303-12. Epub 20160802. doi: 10.1016/j.media.2016.07.007. PubMed PMID: 27497072.
19. Becker AS, Marcon M, Ghafoor S, Wurnig MC, Frauenfelder T, Boss A. Deep Learning in Mammography: Diagnostic Accuracy of a Multipurpose Image Analysis Software in the Detection of Breast Cancer. *Invest Radiol*. 2017;52(7):434-40. doi: 10.1097/RLI.0000000000000358. PubMed PMID: 28212138.
20. Casellas-Grau A, Vives J, Font A, Ochoa C. Positive psychological functioning in breast cancer: An integrative review. *Breast*. 2016;27:136-68. Epub 20160423. doi: 10.1016/j.breast.2016.04.001. PubMed PMID: 27113230.
21. Dromain C, Boyer B, Ferré R, Canale S, Delalogue S, Balleyguier C. Computed-aided diagnosis (CAD) in the detection of breast cancer. *Eur J Radiol*. 2013;82(3):417-23. Epub 20120830. doi: 10.1016/j.ejrad.2012.03.005. PubMed PMID: 22939365.
22. Gichoya JW, Banerjee I, Bhimireddy AR, Burns JL, Celi LA, Chen LC, et al. AI recognition of patient race in medical imaging: a modelling study. *Lancet Digit Health*. 2022;4(6):e406-e14. Epub 20220511. doi: 10.1016/S2589-7500(22)00063-2. PubMed PMID: 35568690; PubMed Central PMCID: PMC9650160.
23. Chen HL, Zhou MQ, Tian W, Meng KX, He HF. Effect of Age on Breast Cancer Patient Prognoses: A Population-Based Study Using the SEER 18 Database. *PLoS One*. 2016;11(10):e0165409. Epub 20161031. doi: 10.1371/journal.pone.0165409. PubMed PMID: 27798652; PubMed Central PMCID: PMC5087840.
24. Seyyed-Kalantari L, Liu G, McDermott M, Chen IY, Ghassemi M. CheXclusion: Fairness gaps in deep chest X-ray classifiers. *Pac Symp Biocomput*. 2021;26:232-43. PubMed PMID: 33691020.
25. Jeong JJ, Vey BL, Bhimireddy A, Kim T, Santos T, Correa R, et al. The EMory BrEast Imaging Dataset (EMBED): A Racially Diverse, Granular Dataset of 3.4 M Screening and Diagnostic Mammographic Images. *Radiology: Artificial Intelligence*. 2023;e220047.
26. Liberman L, Menell JH. Breast imaging reporting and data system (BI-RADS). *Radiol Clin North Am*. 2002;40(3):409-30, v. doi: 10.1016/s0033-8389(01)00017-3. PubMed PMID: 12117184.
27. Szegedy C, Vanhoucke V, Ioffe S, Shlens J, Wojna Z. Rethinking the inception architecture for computer vision. *Proceedings of the IEEE conference on computer vision and pattern recognition* 2016. p. 2818-26.
28. Simonyan K, Zisserman A. Very Deep Convolutional Networks for Large-Scale Image Recognition. *arXiv preprint arXiv:14091556*. 2014.
29. He K, Zhang X, Ren S, Sun J. Identity mappings in deep residual networks. *Computer Vision—ECCV 2016: 14th European Conference; Amsterdam, The Netherlands: Springer International Publishing.; 2016. p. 630-45*.
30. He K, Zhang X, Ren S, Sun J. Deep residual learning for image recognition. *Proceedings of the IEEE conference on computer vision and pattern recognition*. 2016:770-8.

31. Chan HP, Samala RK, Hadjiiski LM, Zhou C. Deep Learning in Medical Image Analysis. *Adv Exp Med Biol.* 2020;1213:3-21. doi: 10.1007/978-3-030-33128-3_1. PubMed PMID: 32030660; PubMed Central PMCID: PMC7442218.
32. Deng J, Wei D, Socher R, Li L-J, Li K, Fei-fei L. Imagenet: A large-scale hierarchical image database. 2009 IEEE conference on computer vision and pattern recognition. 2009:248-55.
33. Agarap AF. Deep Learning using Rectified Linear Units (ReLU). arXiv preprint arXiv. 2018;1803.08375.
34. Han J, Moraga C, editors. The influence of the sigmoid function parameters on the speed of backpropagation learning. *From Natural to Artificial Neural Computation: International Workshop on Artificial Neural Networks; 1995; Malaga-Torremolinos, Spain: Springer Berlin Heidelberg.*
35. Shahriari B, Swersky K, Wang Z, Adams RP, De Freitas N. Taking the human out of the loop: A review of Bayesian optimization. *Proceedings of the IEEE; 2015. p. 148-75.*

Table 1: Characteristics of Image Patches Used for Model Development.

Characteristics	Count (Percentage)			
	Total	Training Set	Validation Set	Testing Set
All patches	52,444(100%)	29,144(100%)	9,910(100%)	13,390(100%)
Label				
Positive	24,166(46.1%)	13,461(46.2%)	4,563(46.0%)	6,142(45.9%)
Negative	28,278(53.9%)	15,683(53.8%)	5,347(54.0%)	7,248(54.1%)
BI-RADS				
0-additional imaging needed	38,293(73.0%)	21,318(73.1%)	7,212(72.8%)	9,763(72.9%)
1-negative or 2-benign	14,151(27.0%)	7,826(26.9%)	2,698(27.2%)	3,627(27.1%)
Race				
African American or Black	22,321(42.5%)	12,483(42.8%)	4,137(41.7%)	5,701(42.6%)
Caucasian or White	21,273(40.6%)	11,649(40.0%)	4,140(41.8%)	5,484(40.9%)
Other	8,850(16.9%)	5,012(17.2%)	1,633(16.5%)	2,205(16.5%)
Age Group				
<50	16,387(31.2%)	9,184(31.5%)	3,293(33.2%)	3,910(29.2%)
50-60	14,775(28.2%)	8,138(27.9%)	2,811(28.4%)	3,826(28.6%)
60-70	12,490(23.8%)	6,965(23.9%)	2,240(22.6%)	3,285(24.5%)
>70	8,792(16.8%)	4,857(16.7%)	1,566(15.8%)	2,369(17.7%)
BI-RADS Density				
A-Almost entirely fatty	6,050(11.5%)	3,218(11.0%)	1,166(11.8%)	1,666(12.4%)
B-Scattered areas of fibroglandular density	18,544(35.4%)	10,275(35.3%)	3,348(33.8%)	4,921(36.8%)
C-Heterogeneously dense	23,218(44.3%)	12,682(43.5%)	4,310(43.5%)	6,226(46.5%)
D-Extremely dense	4,632(8.8%)	2,969(10.2%)	1,086(10.9%)	577(4.3%)
Pathology				
Cancer	1,147(2.2%)	739(2.5%)	233(2.3%)	175(1.3%)
Benign	3,495(6.7%)	2,025(7.0%)	662(6.7%)	808(6.0%)
Never Biopsied	47,802(91.1%)	26,380(90.5%)	9,015(91.0%)	12,407(92.7%)
Image Finding				
Mass				1,774(13.2%)
Asymmetry				5,372(40.1%)
AD				579(4.3%)
Calcification				2,502(18.7%)

AD = Architectural Distortion, BI-RADS = Breast Imaging Reporting and Data System

Note: Due to the structure of the dataset, imaging features prevalence could only be calculated for the test set in which images contained a single ROI. Images in the training and validation dataset may contain multiple ROIs so exact prevalence could not be calculated.

Table 2: Comparison of multiple standard convolutional neural network (CNN) models for binary patch classification. We found ResNet152V2 achieved the highest performance and was therefore used for the remainder of experiments.

Model	Accuracy	AUC	Recall	Precision	F1 Score
VGG16	0.794	0.881	0.794	0.766	0.780
InceptionV3	0.906	0.967	0.886	0.907	0.897
ResNet50V2	0.918	0.968	0.912	0.909	0.910
ResNet152V2	0.926	0.975	0.927	0.912	0.919

AUC = Area Under the receiver operative characteristics Curve

Table 3: Classification model performance both overall and by subgroup.

Group	Accuracy	AUC	Recall	Precision	F1 score	FNR
Overall						
Train	0.984	0.998	0.984	0.983	0.983	0.016
Validation	0.926	0.967	0.915	0.925	0.920	0.085
Test	0.926±0.006	0.975±0.003	0.927±0.008	0.912±0.010	0.919±0.006	0.073±0.008
Race						
White	0.922±0.009	0.972±0.005	0.918±0.013	0.902±0.016	0.910±0.011	0.082±0.013
Black	0.927±0.009	0.976±0.005	0.931±0.012	0.914±0.015	0.922±0.010	0.069±0.012
Other	0.928±0.015	0.978±0.007	0.938±0.020	0.926±0.020	0.932±0.014	0.062±0.020
Age						
<50	0.916±0.012	0.970±0.007	0.922±0.014	0.919±0.016	0.920±0.011	0.078±0.014
50-60	0.926±0.011	0.977±0.005	0.930±0.017	0.915±0.018	0.922±0.012	0.070±0.017
60-70	0.933±0.013	0.976±0.006	0.932±0.017	0.916±0.022	0.924±0.016	0.068±0.017
> 70	0.930±0.014	0.975±0.008	0.928±0.023	0.882±0.031	0.904±0.021	0.072±0.023
BI-RADS Density						
A	0.950±0.016	0.977±0.013	0.924±0.040	0.825±0.069	0.871±0.044	0.076±0.040
B	0.942±0.009	0.982±0.004	0.942±0.012	0.936±0.014	0.939±0.009	0.058±0.012
C	0.910±0.008	0.966±0.005	0.920±0.012	0.906±0.013	0.913±0.009	0.080±0.012
D	0.877±0.036	0.953±0.021	0.899±0.046	0.882±0.047	0.891±0.034	0.101±0.046
Pathology						
Never Biopsied	0.925±0.006	0.974±0.003	0.925±0.008	0.908±0.010	0.916±0.007	0.075±0.008
Benign	0.937±0.019	0.977±0.010	0.955±0.022	0.943±0.027	0.949±0.016	0.045±0.022
Cancer	0.930±0.049	0.980±0.023	0.938±0.063	0.957±0.052	0.947±0.042	0.062±0.063
Image Findings						
Mass	0.931±0.017	0.980±0.008	0.949±0.022	0.896±0.029	0.922±0.020	0.051±0.022
Asymmetry	0.930±0.009	0.977±0.005	0.937±0.010	0.942±0.011	0.939±0.008	0.063±0.010
AD	0.826±0.032	0.914±0.034	0.810±0.040	0.939±0.027	0.869±0.026	0.190±0.040
Calcification	0.920±0.016	0.974±0.008	0.939±0.018	0.904±0.022	0.921±0.016	0.061±0.018

AD = Architectural Distortion, AUC = Area Under the receiver operative characteristics Curve, BI-RADS = Breast Imaging Reporting and Data System, FNR = False Negative Rate

Table 4: Image level performance of classifier with risk ratio of misclassification by subgroup

Variables	Coefficients	Odds Ratio	Risk Ratio	P-Value	Control Group
Black	-0.067	0.935	0.959	0.454	White
Other	-0.221	0.802	0.867	0.058	White
50-60yr	-0.075	0.928	0.95	0.456	<50yr
60-70yr	-0.109	0.897	0.929	0.336	<50yr
>70yr	0.018	1.018	1.012	0.894	<50yr
BI-RADS density B	0.025	1.025	1.024	0.908	BI-RADS density A
BI-RADS density C *	0.539	1.714	1.649	0.010	BI-RADS density A
BI-RADS density D *	0.767	2.154	2.026	0.003	BI-RADS density A
Benign	-0.273	0.761	0.968	0.087	Never Biopsied
Cancer	-0.183	0.833	0.98	0.565	Never Biopsied
Mass	-0.068	0.934	0.991	0.647	No Mass
Asymmetry	-0.086	0.918	0.956	0.446	No Asymmetry
AD *	0.701	2.016	1.026	0.000	No AD
Calcification	-0.039	0.962	0.992	0.767	No Calcification

*: Statistically significant, $p \leq .05$; AD = Architectural Distortion, BI-RADS = Breast Imaging Reporting and Data System

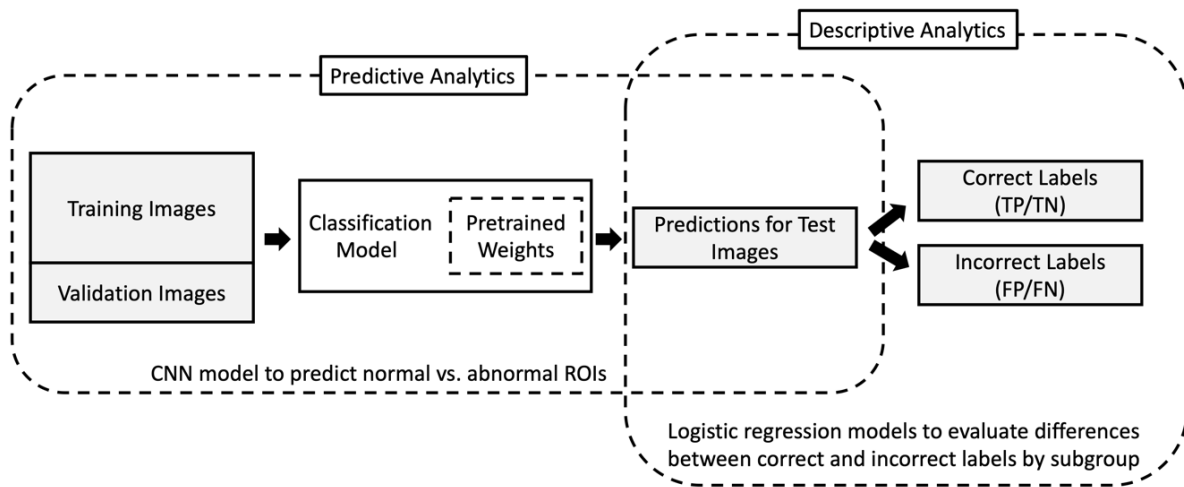


Figure 1: Experimental overview with two main components. Predictive analytics which involve training of a deep learning model to differentiate between normal and abnormal patches on mammography deep learning model training and descriptive analytics which involves evaluation of subgroup model performance. TP = True Positive, TN = True Negative, FP = False Positive, FN = False Negative.

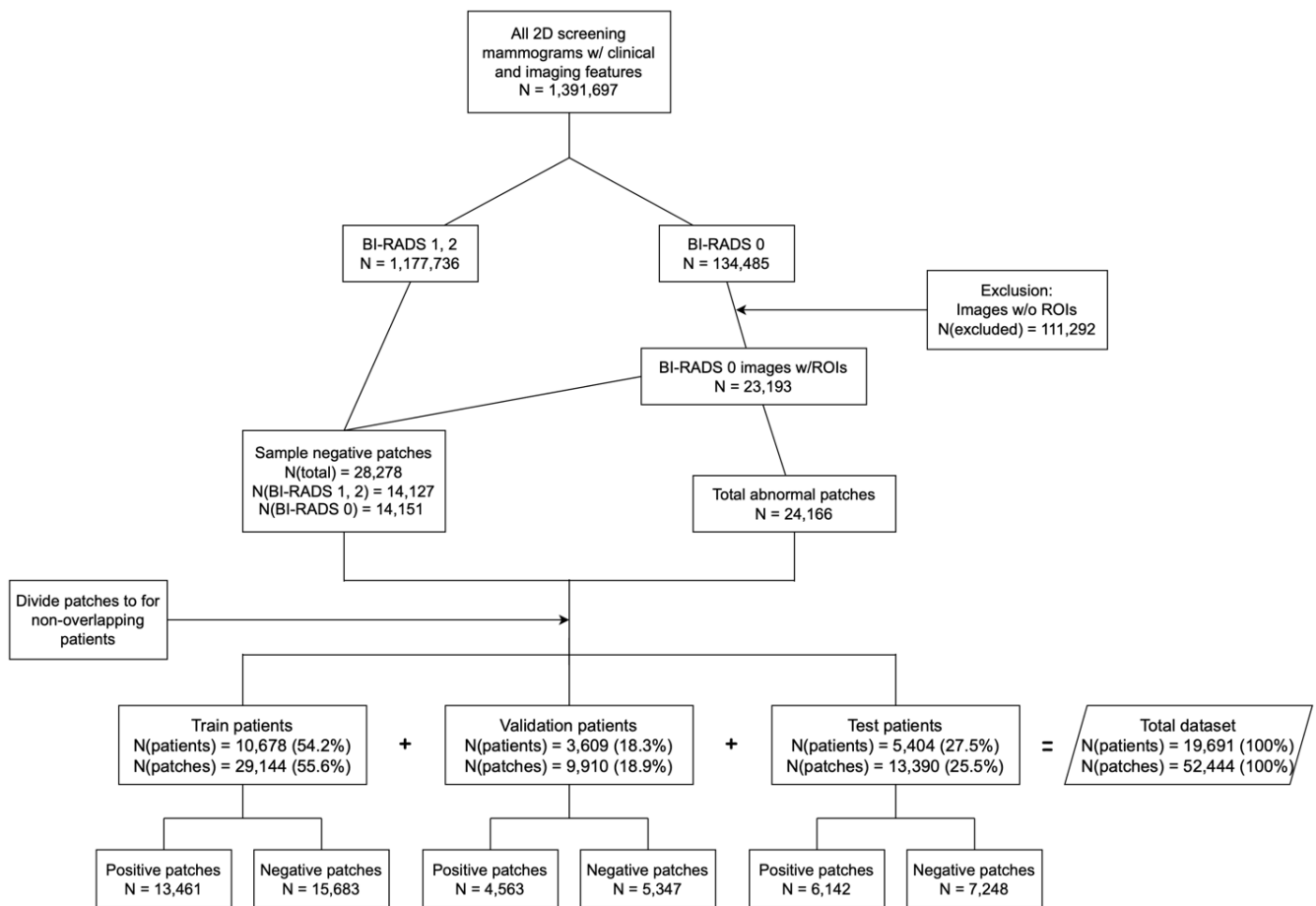


Figure 2: Flow chart of dataset creation. Positive patches are extracted from BI-RADS 0 images using annotations created by the radiologist at time of interpretation. Negative patches are extracted from BI-RADS 1 and 2 images and areas outside of the radiologist ROI on BI-RADS 0 images. Similar numbers of negative and positive patches were used in this experiment. Training, validation, and test sets were separated by patient to avoid data leakage. BI-RADS = Breast Imaging Reporting and Data System.

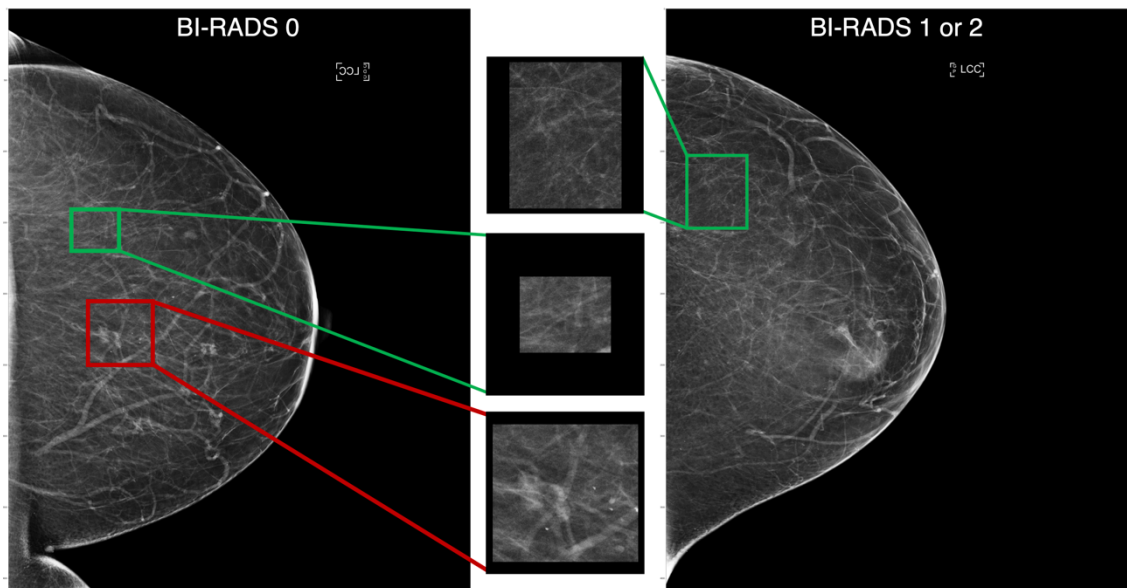


Figure 3: Example of positive and negative patch generation. The patch highlighted in the red box represents an abnormality detected by the radiologist on a BI-RADS 0 exam. The patches highlighted in green represent randomly selected other patches from BI-RADS 0 images (left) and negative images (right). The patches were cropped, centered, and padded with 0 pixels to be 512×512 pixels. Patches larger than 512×512 pixels were downsampled and then padded. BI-RADS = Breast Imaging Reporting and Data System.

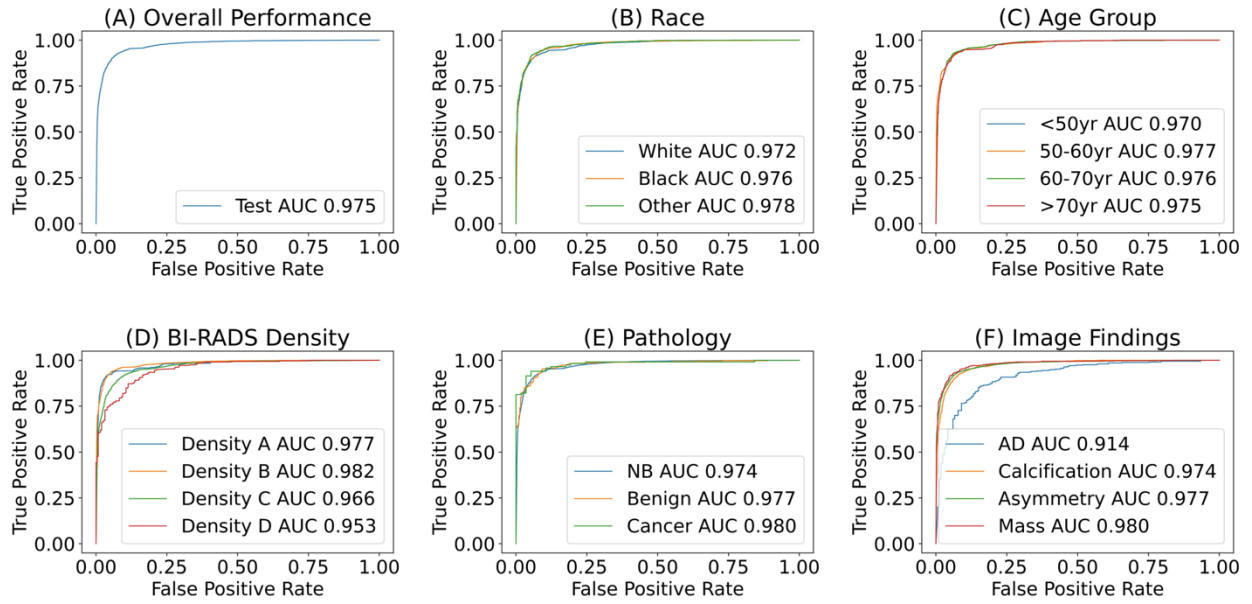


Figure 4: Receiver operating characteristic curves of the whole test set **(A)**, and by subgroups – race **(B)**, age group **(C)**, BI-RADS density **(D)**, pathology **(E)**, and image findings **(F)**. AUC = Area Under the receiver operative characteristics Curve, BI-RADS = Breast Imaging Reporting and Data System, NB = Never Biopsied.

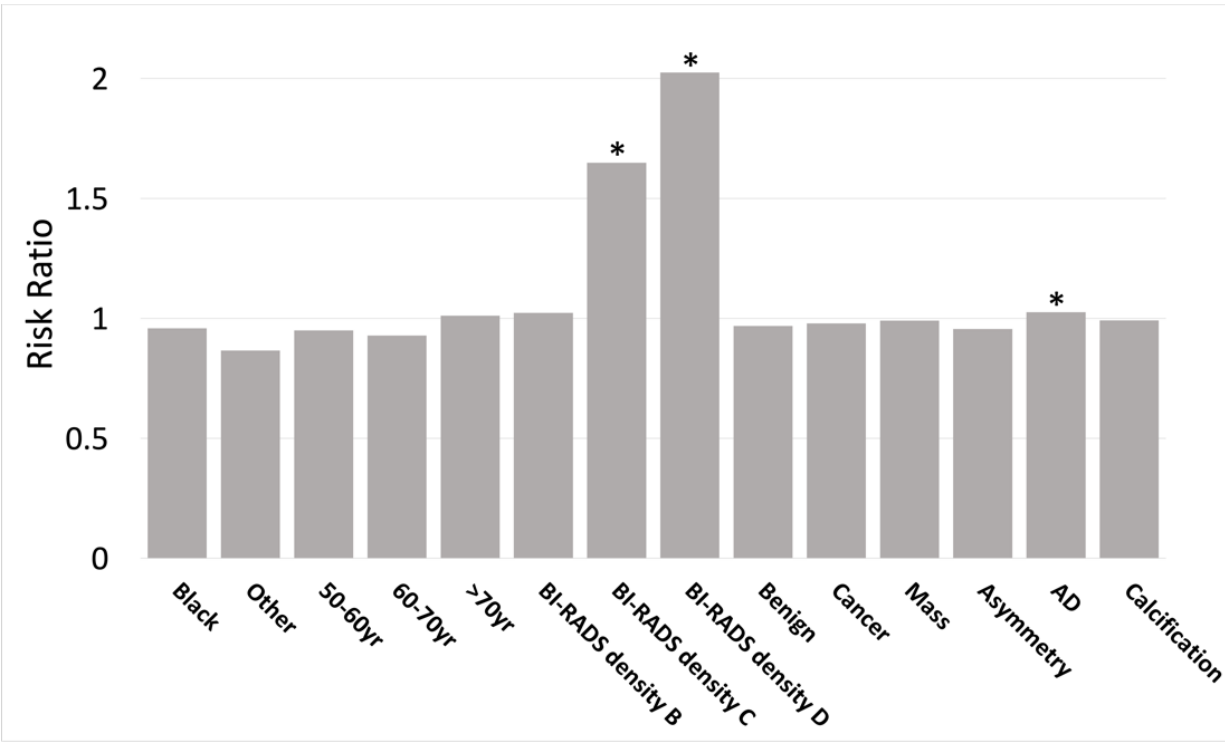


Figure 5: Risk ratio for misclassification of an image by demographic or presence of an imaging feature. In this evaluation, an image was considered misclassified if at least one patch was incorrectly classified (false positive or false negative). The risks of misclassification were higher in patients with breast tissue densities C and D as compared to density A and for patients with architectural distortion (AD) as compared to other imaging findings. BI-RADS = Breast Imaging Reporting and Data System.

*: statistical significance was set at $p \leq .05$

Supplemental Table 1: One-sided unpaired *t* test results comparing AUCs across subgroups.

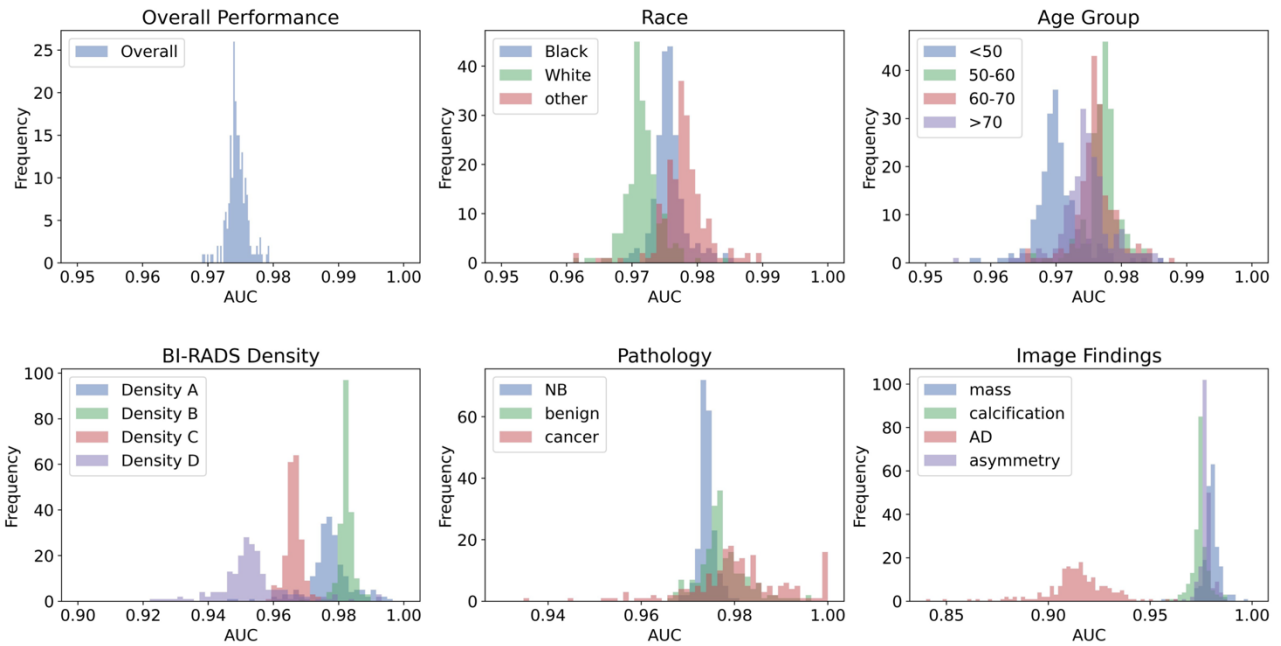
Category	Subgroup 1	Subgroup 2	<i>t</i> -statistic	<i>P</i> value
Race	Black	White	16.645	<0.001
	Black	other	-6.472	<0.001
	White	other	-19.292	<0.001
Age group	<50	50-60	-22.524	<0.001
	<50	60-70	-17.527	<0.001
	<50	>70	-12.310	<0.001
	50-60	60-70	3.700	<0.001
	50-60	>70	7.171	<0.001
	60-70	>70	3.653	<0.001
BIRADS Density	A	B	-10.149	<0.001
	A	C	21.700	<0.001
	A	D	26.986	<0.001
	B	C	70.528	<0.001
	B	D	38.223	<0.001
	C	D	16.802	<0.001
Pathology	never biopsied	benign	-8.735	<0.001
	never biopsied	cancer	-7.552	<0.001
	benign	cancer	-3.286	<0.001
Image findings	mass	calcification	14.734	<0.001
	mass	AD	52.673	<0.001
	mass	asymmetry	8.680	<0.001
	calcification	AD	48.160	<0.001
	calcification	asymmetry	-8.906	<0.001
	AD	asymmetry	-51.166	<0.001

The significance level was set at $p \leq .025$. Abbreviations: AD = Architectural Distortion, BIRADS = Breast Imaging Reporting and Data System. Note: Results were generated using 200 bootstraps of the test dataset.

Supplemental Table 2: Pathology outcomes of image findings in test set patches.

Image Findings	Cancer	Benign	Never Biopsied
Mass	8	75	1,693
Asymmetry	97	390	2,023
AD	19	50	510
Calcification	82	265	5,025

AD = Architectural Distortion



Supplemental Figure 1: Histogram demonstrating distribution of AUCs of the test set with 200 bootstraps. Most subgroups showed small, but statistically significant differences in performance across subgroups. AD = Architectural Distortion, AUC = Area Under the receiver operative characteristics Curve, BI-RADS = Breast Imaging Reporting and Data System, NB = Never Biopsied.